

2. F. Pampaloni, E. G. Reynaud, E. H. K. Stelzer, *Nat. Rev. Mol. Cell Biol.* **8**, 839 (2007).
3. D. E. Ingber, *FASEB J.* **20**, 811 (2006).
4. G. M. Whitesides, E. Ostuni, S. Takayama, X. Y. Jiang, D. E. Ingber, *Annu. Rev. Biomed. Eng.* **3**, 335 (2001).
5. A. Khademhosseini, R. Langer, J. Borenstein, J. P. Vacanti, *Proc. Natl. Acad. Sci. U.S.A.* **103**, 2480 (2006).
6. J. El-Ali, P. K. Sorger, K. F. Jensen, *Nature* **442**, 403 (2006).
7. I. Meyvantsson, D. J. Beebe, *Annu. Rev. Anal. Chem.* **1**, 423 (2008).
8. M. Shin *et al.*, *Biomed. Microdevices* **6**, 269 (2004).
9. J. W. Song *et al.*, *Anal. Chem.* **77**, 3993 (2005).
10. M. T. Lam, Y. C. Huang, R. K. Birla, S. Takayama, *Biomaterials* **30**, 1150 (2009).
11. K. Jang, K. Sato, K. Igawa, U. I. Chung, T. Kitamori, *Anal. Bioanal. Chem.* **390**, 825 (2008).
12. D. Huh *et al.*, *Proc. Natl. Acad. Sci. U.S.A.* **104**, 18886 (2007).
13. A. Carraro *et al.*, *Biomed. Microdevices* **10**, 795 (2008).
14. P. J. Lee, P. J. Hung, L. P. Lee, *Biotechnol. Bioeng.* **97**, 1340 (2007).
15. M. J. Powers *et al.*, *Biotechnol. Bioeng.* **78**, 257 (2002).
16. S. R. Khetani, S. N. Bhatia, *Nat. Biotechnol.* **26**, 120 (2008).
17. J. W. Park, B. Vahidi, A. M. Taylor, S. W. Rhee, N. L. Jeon, *Nat. Protoc.* **1**, 2128 (2006).
18. S. G. Harris, M. L. Shuler, *Biotechnol. Bioprocess Eng.* **8**, 246 (2003).
19. G. J. Mahler, M. B. Esch, R. P. Glahn, M. L. Shuler, *Biotechnol. Bioeng.* **104**, 193 (2009).
20. R. Baudoin, L. Griscorn, M. Monge, C. Legallais, E. Leclerc, *Biotechnol. Prog.* **23**, 1245 (2007).
21. K. J. Jang, K. Y. Suh, *Lab Chip* **10**, 36 (2010).
22. S. Takayama *et al.*, *Adv. Mater.* **13**, 570 (2001).
23. I. Frerking, A. Günther, W. Seeger, U. Pison, *Intensive Care Med.* **27**, 1699 (2001).
24. K. J. Kim, A. B. Malik, *Am. J. Physiol. Lung Cell. Mol. Physiol.* **284**, L247 (2003).
25. K. G. Birukov *et al.*, *Am. J. Physiol. Lung Cell. Mol. Physiol.* **285**, L785 (2003).
26. T. Iba, B. E. Sumpio, *Microvasc. Res.* **42**, 245 (1991).
27. C. K. Thodeti *et al.*, *Circ. Res.* **104**, 1123 (2009).
28. J. G. Wagner, R. A. Roth, *Pharmacol. Rev.* **52**, 349 (2000).
29. M. I. Hermans *et al.*, *Cell Tissue Res.* **336**, 91 (2009).
30. D. Wong, K. Dorovini-Zis, *J. Neuroimmunol.* **39**, 11 (1992).
31. A. Nel, T. Xia, L. Mädler, N. Li, *Science* **311**, 622 (2006).
32. V. L. Colvin, *Nat. Biotechnol.* **21**, 1166 (2003).
33. G. Oberdörster, E. Oberdörster, J. Oberdörster, *Environ. Health Perspect.* **113**, 823 (2005).
34. W. S. Lin, Y. W. Huang, X. D. Zhou, Y. F. Ma, *Toxicol. Appl. Pharmacol.* **217**, 252 (2006).
35. D. Napierska *et al.*, *Small* **5**, 846 (2009).
36. R. Merget *et al.*, *Arch. Toxicol.* **75**, 625 (2002).
37. N. L. Mills *et al.*, *Nat. Clin. Pract. Cardiovasc. Med.* **6**, 36 (2009).
38. A. M. Bilek, K. C. Dee, D. P. Gaver 3rd, *J. Appl. Physiol.* **94**, 770 (2003).
39. H. W. Sill *et al.*, *Am. J. Physiol.* **268**, H535 (1995).
40. A. Sin *et al.*, *Biotechnol. Prog.* **20**, 338 (2004).
41. C. Zhang, Z. Q. Zhao, N. A. Abdul Rahim, D. van Noort, H. Yu, *Lab Chip* **9**, 3185 (2009).
42. We thank C. K. Thodeti for his help with ROS assays; G. M. Whitesides and P. Cherukuri for providing carbon nanotubes, gold nanoparticles, and helpful comments; N. Korin for helpful discussions; R. Ruch for providing alveolar epithelial cells; R. Mannix for his imaging assistance; and M. Butte for help with neutrophil isolation. This work was supported by grants from NIH (R01-ES016665), the American Heart Association (0835618D), the Department of Defense (W81XWH-05-1-0115), and the Wyss Institute for Biologically Inspired Engineering at Harvard University; D.H. is a recipient of a Wyss Technology Development Fellowship, and D.E.I. is a recipient of a Department of Defense Breast Cancer Innovator Award. A patent on the device described is pending.

Supporting Online Material

www.sciencemag.org/cgi/content/full/328/5986/1662/DC1

Materials and Methods

SOM Text

Figs. S1 to S11

Table S1

References

Movies S1 to S9

16 February 2010; accepted 7 May 2010

10.1126/science.1188302

REPORTS

4D Electron Tomography

Oh-Hoon Kwon and Ahmed H. Zewail*

Electron tomography provides three-dimensional (3D) imaging of noncrystalline and crystalline equilibrium structures, as well as elemental volume composition, of materials and biological specimens, including those of viruses and cells. We report the development of 4D electron tomography by integrating the fourth dimension (time resolution) with the 3D spatial resolution obtained from a complete tilt series of 2D projections of an object. The different time frames of tomograms constitute a movie of the object in motion, thus enabling studies of nonequilibrium structures and transient processes. The method was demonstrated using carbon nanotubes of a bracelet-like ring structure for which 4D tomograms display different modes of motion, such as breathing and wiggling, with resonance frequencies up to 30 megahertz. Applications can now make use of the full space-time range with the nanometer-femtosecond resolution of ultrafast electron tomography.

For nearly a century, the determination of three-dimensional (3D) structures of a crystalline specimen, with redundancy in the repeating units of the architecture, has primarily depended on x-ray and electron-based methods. Recently, with the combination of electron microscopy techniques and fast computation methods, electron tomography has become a powerful tool for 3D structural determination of nanoscopic noncrystalline materials (1, 2) and biolog-

ical assemblies such as viruses, bacteria, and cells (3–5). Historically, several initial advances were made (5), but the first examples of the approach were published with different variants in the 1960s: reconstruction of 3D biostructures (of high symmetry) from one or more projections (6, 7), reconstruction of an asymmetric protein structure from a sufficient number of projections (8), and average reprojection calculated from a tilt series of images (9). However, decades of advances in computation methods were required to bring the field into the state of the art in high-resolution electron tomography with applications in many fields (10–12), which include the impressive methods of energy-filtering for mapping a specific element or site (13–16) and the use

of the high-angular annular dark field (HAADF) for suppressing the diffraction contrast of crystalline materials (17, 18). In all of these studies, the tomograms obtained are those of a static object representing the time-averaged equilibrium state of the structure.

To visualize the dynamics, the dimension of time must be integrated into any electron tomogram that spans a whole tilt series. Furthermore, the time resolution in every step must be high enough to capture the motion of the object, ideally reduced to the atomic scale. This simultaneous real-space and real-time resolution can be obtained using ultrafast electron microscopy (UEM) (11, 19). However, in UEM a snapshot represents a time frame of the 2D projection of the object under investigation, making invisible the spatial information in the dimension along the optical axis of the microscope. This is because of the large focus depth in the specimen.

Here, we report the development of 4D electron tomography. The tomograms are constructed from nearly 4000 projections for a whole series of tilt angles and time steps. The methodology is demonstrated in the imaging of multiwalled carbon nanotubes (MWNTs), with the time resolution being independent of the video camera response time of milliseconds, thus enabling the visualization of non-equilibrium, fleeting structures on the femtosecond to millisecond time scale. For the nanotubes, the 4D tomograms in a movie display the mechanical motions and morphological dynamics of the object, a

Physical Biology Center for Ultrafast Science and Technology, Arthur Amos Noyes Laboratory of Chemical Physics, California Institute of Technology, Pasadena, CA 91125, USA.

*To whom correspondence should be addressed. E-mail: zewail@caltech.edu

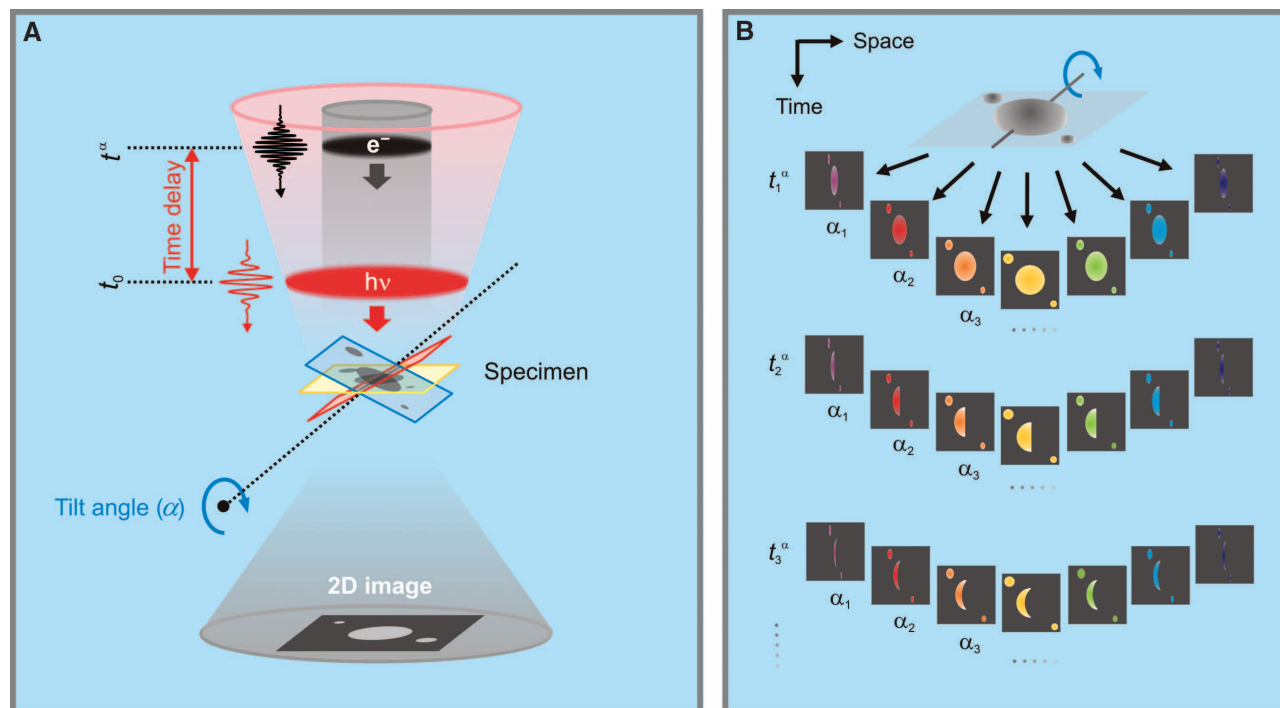


Fig. 1. (A) Schematic representation of time-resolved 4D electron tomography. The heating pulse initiates (at t_0) the structural change and acts as a clocking pulse, whereas the time-delayed electron packet (at t^α), with respect to the clocking pulse, images the structure at a given tilt angle (α). (B) A series of 2D images at various projection angles and time steps are taken to

construct the tomograms. In this work, increments of 1° and scanings from -58° to $+58^\circ$ were used to define α and its range; the time scale ranged from femtoseconds to microseconds. The number of total spatiotemporal projections made was near 4000, and these were used to construct the tomographic movies of the object in motion; see text.

bracelet-like structure. For comparison, the dynamics for the same object were investigated for the 2D projections. The complex structures involved exhibit various resonances of motions after laser-driven impulsive heating, and it is possible to obtain their frequencies and the pertinent segmental structure responsible for their dynamics.

Shown in Fig. 1A is a schematic representation of the approach. In addition to the known methodology of UEM (20, 21), here a specimen-tilt arrangement is configured to enable the recording of various 2D projections of an object at a given time. The frames are taken for each degree of tilt with time steps of femtoseconds or nanoseconds, as dictated by the time scale of the motions involved. The concept is illustrated in Fig. 1B, which depicts the construction of tomograms from the 2D projections at different angles and times. Because of the various dimensions involved, we note that at a given time each 2D projection represents a 3D frame (including time), whereas a 3D tomogram when constructed from all the 2D projections represents a 4D frame.

In these studies, two laser systems were used, depending on the time scale of interest. The structural change was initiated through the use of a heating (clocking) pulse, and the images were recorded using the electron (probing) pulse. The timing was controlled by changing the delay time of the electron pulses relative to the heating pulse, either optically (using a delay stage) in

the femtosecond mode or electronically in the nanosecond mode. Each time frame was constructed stroboscopically in a few seconds. The electrons were accelerated to 200 kV, giving a de Broglie wavelength of 2.5 pm. The data processing and analysis involved extensive computations, as described below.

For the carbon nanotubes used in this study (22), the diffraction contrast in the bright-field images at different tilt angles was nearly absent, thus satisfying the condition for the projection requirement (10)—that is, the contrast in images arises dominantly from changes in specimen density or thickness. Accordingly, we took a series of bright-field images of various 2D projections by single-axis tilting (23) of the specimen and constructed a 3D tomogram at a well-defined time, t_i^α , where i denotes a given time step and α denotes the tilt angle defined with respect to the electron beam. Such tomograms were generated for a whole series of time delays. The stroboscopic buildup of the tomogram is ideal in this configuration, as the specimen returns to the original structure for any α or any i setting.

In generating the tomograms, the tilt series of images was aligned with respect to reference landmarks and a precise tilt axis (24); as in conventional tomography, median filtering was used to assist in the image alignment procedure. By using the iterative algebraic algorithm ART or SIRT (25), the 3D (volume) tomograms were reconstructed from the aligned images. We then used a series of such time frames of 3D tomograms to

make a movie, which displays the temporal evolution of the morphological and mechanical motions. The resonance and local motions become identifiable from changes of volume density selected in the tomograms. Note that the time interval between successive clocking pulses can be chosen to ensure complete heat dissipation and damping out of the mechanical motions before the arrival of each clocking pulse.

In Fig. 2A, we present two time frames of the 3D structures obtained from representative, reconstructed 4D tomograms at $t = 50$ ps (left) and $t = 25$ ns (right); at earlier times, in femtosecond frames, there was no noticeable change. The tomograms show the nanoscale tubular structure and the microscale spiral ring, the “bracelet-like” structure. From the tomographic reconstruction, it can be seen that bright-field imaging reproduced the object structure and that the morphology of the sample is preserved. Cross sections of different carbon nanotubes show that the tubular structure has a diameter of 10 ± 2 nm (Fig. 2B); at this magnification and binning, the single-pixel resolution is 4.6 nm. To confirm the general structure, we also obtained transmission electron microscopy (TEM) images at $\alpha = 0^\circ$ (Fig. 2C). These images—which display the support of the bracelet by other tubes, without a substrate—have features that are consistent with the reconstructed tomograms. At higher magnifications, we find that the thickest tube has an average outer diameter of 55 nm and inner diameter of 12 nm for a hollow channel; a narrower tube

has an outer diameter of 28 nm and an inner diameter of 9 nm. From the tomographic volume reconstruction, the 28-nm tube turned out to be attached to the spiral ring of the 55-nm one (Fig. 2A).

Representative time frames of 2D projections of the nanotubes taken at several delay times are displayed in Fig. 3A (26). At positive times spanning the nanosecond and microsecond time regime, after $t = 0$, visual changes are clear in the difference images (Fig. 3B). With time, the bracelet begins to move after the heating pulse, and with these and other micrographs of equal time steps we made a movie of such mechanical motions (movie S1, covering the period from -100 ns to 1.9 μ s). No noticeable change was observed in images obtained before the arrival of the heating pulse, indicating that the bracelet had returned to its original spatial configuration. Moreover, because each time frame was formed stroboscopically by accumulating $\sim 10^4$ snapshots (at a repetition rate of 3 kHz for a few seconds),

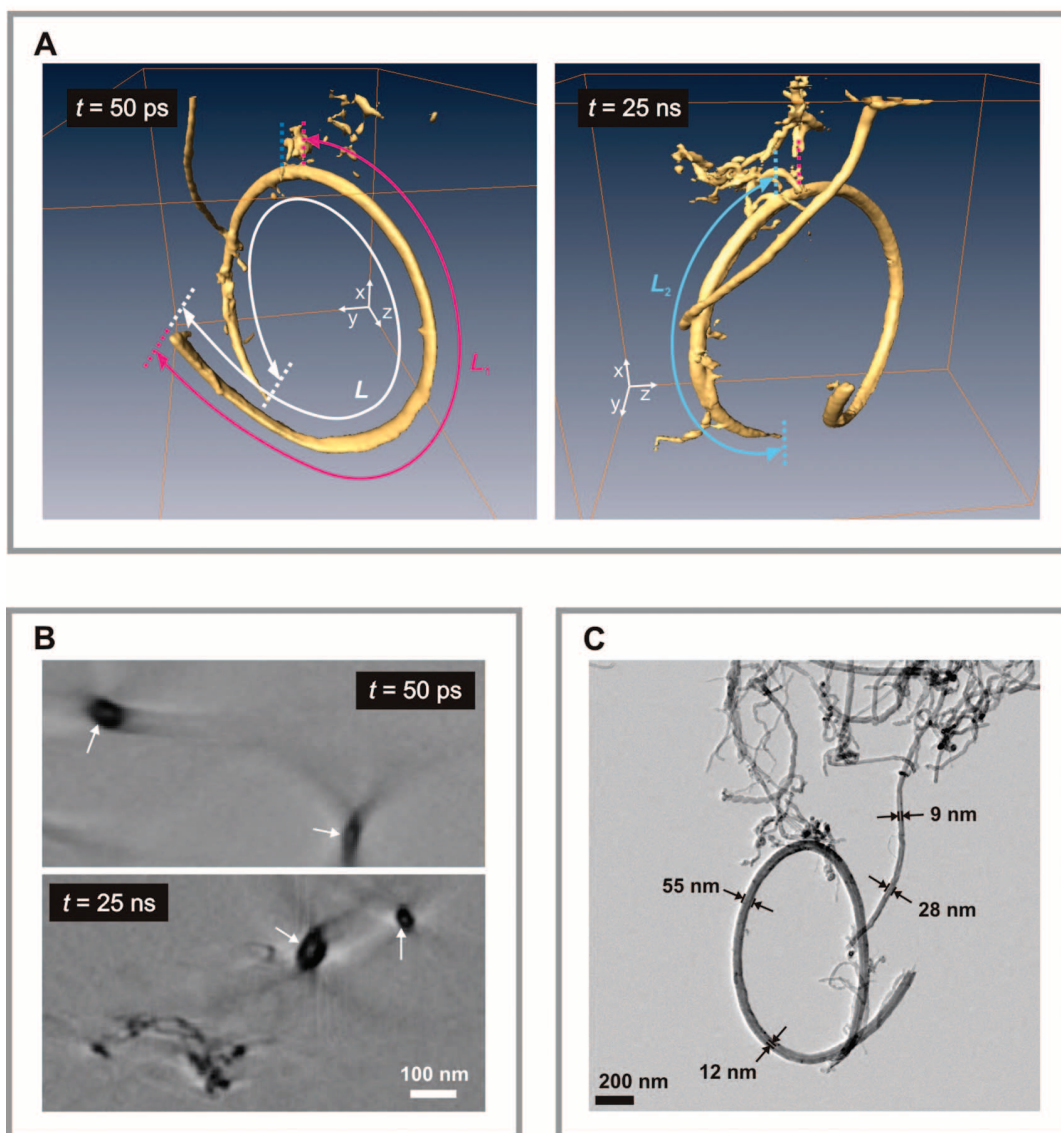
the revealed motion was reversible, reverting to the at-rest position after each heating pulse. There was no sign of structural fatigue or deformation observed during the course of the experiments. The average dose for each 2D projection image was ~ 15 e^-/nm^2 at the maximum number of electrons in the nanosecond pulse; for the femtosecond pulse, this number was lower by two orders of magnitude. The total dose for the entire tomographic recording was $\leq 10^5$ e^-/nm^2 , which is at least two orders of magnitude smaller than that reported to cause deformation of MWNTs (27, 28).

Figure 3C depicts the temporal behavior obtained from 2D images, as identified by the arrows shown in the frame at negative time (Fig. 3A). Plotted is the displacement from the original position along the transverse directions of the tube, which exhibits the oscillatory behavior shown. The oscillations have well-defined resonance frequencies of 29.9, 13.5, 5.9, and 3.5 MHz, and some near 21 MHz, as quantified in Fig. 3D by taking the fast Fourier transform (FFT) of the dis-

placements. After 1 μ s, the two prominent modes at 13.5 and 3.5 MHz survive. Because the images are 2D representations of an originally imaged 3D structure in motion, it is difficult to fully elucidate the nature of the modes involved, which raises the question of whether these resonances result from the wiggling around the anchored tubes or from the breathing resonance of the ring.

Figure 4, A and B, shows the evolution of 4D tomograms of the object for two sets of view angles at representative early time frames and at longer times, respectively. At each time, such tomograms were generated from the sets of 2D projections taken at a series of tilt angles with steps of 1° , from -58° to $+58^\circ$ (29). For comparison, we also constructed movies of 2D projections taken at different tilt angles: -55° , 0° , and $+55^\circ$ (movie S1). From the reconstructed 4D tomograms in Fig. 4, it is possible to visualize the complicated motions and to dissect some normal modes in 3D coordinates. There are two prominent time scales of the motion. At early

Fig. 2. Tomograms and images resolved in time. **(A)** Representative time frames of 3D volume images taken at $t = 50$ ps and 25 ns for the MWNT specimen. The bracelet shape (radius 620 nm) and the detailed tubular morphology are displayed; from the 3D volume models, the length of the ring (L) was measured to be 4.4 μm . Around the anchored region of the ring, L_1 and L_2 are the lengths of the long and short segments, respectively. The 3D isosurface rendering was made with the Amira visualization program. **(B)** Cross section of tomographic images. Shown are 4.6 -nm-thick 2D slices in the xy plane, perpendicular to the optical axis, at $t = 50$ ps (top) and 25 ns (bottom). The dark regions indicated by arrows represent nanometer-thick carbon walls; the light area is the vacant space in the tomograms. Tubular features with hollow channels of diameter ~ 10 nm are well resolved. **(C)** TEM image of a MWNT specimen. A typical projection image at $\alpha = 0^\circ$ is given with the dimensions indicated. Despite the initial femtosecond excitation, all motions in the object begin on the picosecond time scale because of the nature of structural change (26).



times (Fig. 4A), the volumes in black describe the original configuration of the object, whereas those in beige depict the new configuration displaced from the original position. One can identify the early-time resonance “breathing-type” motion, because by 75 ns the reversal for the volume density of the bracelet was obtained. At longer times, the bracelet resonates on a slower time scale; the reversal of the motion is clear, as highlighted by changes in color coding and by the directions of arrows shown in Fig. 4B.

Specifically, at $t = 5$ ns, the two ends of the ring begin to move (Fig. 4A), and in 15 ns, the displacement of the specimen from the at-rest position is observed for the whole ring. At $t = 30$ ns, the bending motion of the ring is revealed; the two ends move in the same direction, whereas the middle part of the ring moves in the opposite direction. This bent-ring configuration restores the structure nearly to its original position at $t = 75$ ns. The time scale of motions revealed in the tomograms corresponds to those obtained independently using 2D images at a given tilt angle, such as $\alpha = 0^\circ$ (insets, Fig. 4A). On the microsec-

ond time scale (e.g., from 1950 to 2090 ns), the bracelet wiggles, as evident from changes in the volume density, which show displacement in the same direction (Fig. 4B). In the next 140 ns, the direction of motion is reversed, revealing that the resonance motion is a wiggling of the whole bracelet around the anchored position.

The breathing period of ~ 70 ns corresponds to the 13.5-MHz resonance obtained in the FFT analysis (Fig. 3D). To estimate Young’s modulus (Y) of the tube, we assumed that the frequencies of the open ring are derivable from a beam undergoing bending motions, similar to a previous analysis of nanotubes (30). This assumption is justified when one notices the direction of displacement at, for example, 30 ns in Fig. 4A. The Euler-Bernoulli equation (31) for elastic beams with natural frequencies, f_n , is given by

$$f_n = \frac{\beta_n^2}{8\pi L^2} \sqrt{\frac{(D_o^2 + D_i^2)Y}{\rho}} \quad (1)$$

where L , D_o , D_i , and ρ denote the length, the outer diameter, the inner diameter, and the density of

the MWNT, respectively; β_n is a constant for the n th mode. For simplicity, the free-ends boundary condition was adopted with $\beta_1 = 4.730$.

For $D_o = 55$ nm, $D_i = 12$ nm, and $L = 4.4$ μm , all values were easily retrieved from the images, and using the observed value of $f_1 = 13.5$ MHz, Young’s modulus was calculated to be 61 GPa. This value is in the range reported for carbon nanotubes, from ~ 1 TPa for $D_o < 10$ nm to ~ 100 GPa for tubes of larger diameter (30, 32); for bent tubes, smaller Y values are expected because of wrinkles or ripples on the inner arc. Knowing that $Y = 61$ GPa, and using the boundary condition of a clamped-free beam ($\beta_1 = 1.875$), we can deduce the frequencies for segments of the bracelet; for $L_1 = 1.4$ μm and $L_2 = 2.8$ μm (Fig. 2A), one obtains 5.3 and 21.4 MHz, respectively. These frequencies are in agreement with those obtained (5.9 and ~ 21 MHz) in the FFT analysis (Fig. 3D), supporting the assignment of $f_1 = 13.5$ MHz to the global motion of the ring and the others to local ones. The tomographic visualization in Fig. 4B indicates that the oscillation at 3.5 MHz (period = 300 ns) is

Fig. 3. Dynamics of 2D image projections. (A) Snapshots of images recorded stroboscopically at different time delays, as indicated at the upper right of each image. (B) Difference images relative to the frame at $t = -50$ ns, showing projected motions of the MWNT specimen. In the difference images, the regions of white or black indicate the motions involved, whereas the gray regions indicate that the contrast is unchanged from that of the reference frame. Scale bars, 200 nm. (C) Oscillatory motions from the time-dependent displacements along three representative transverse cross sections of the MWNT specimen; they are indicated as arrows in the image at $t = -50$ ns, with the color code indicated. (D) FFTs of the displacements in the time regime of 0 to 4.9 μs with a sampling rate of 10 ns for each of the displacements shown. As such, the tomograms would decipher 4D dynamical structures from matrix-isolated conformational structures in cryoelectron microscopy (37).

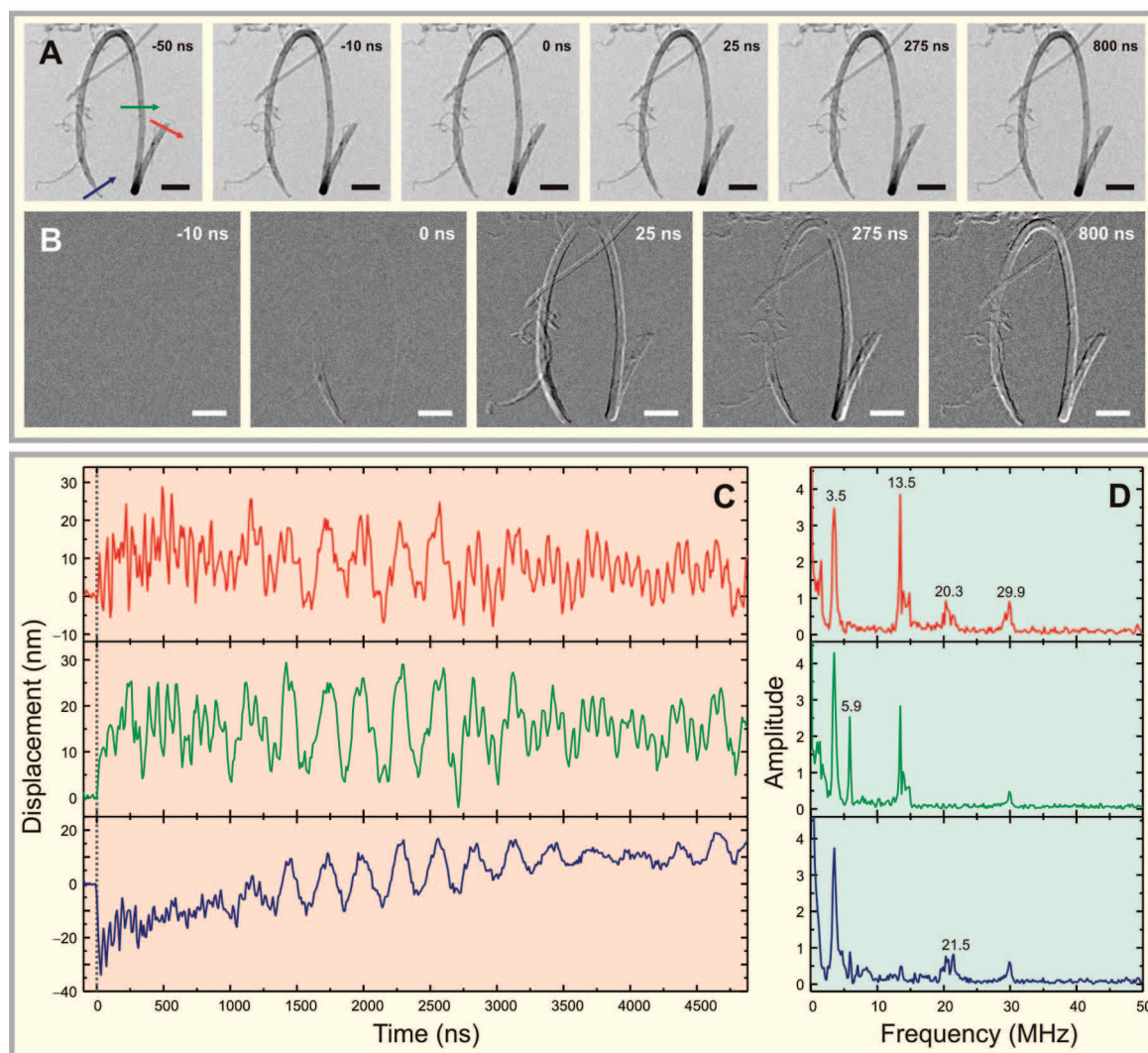
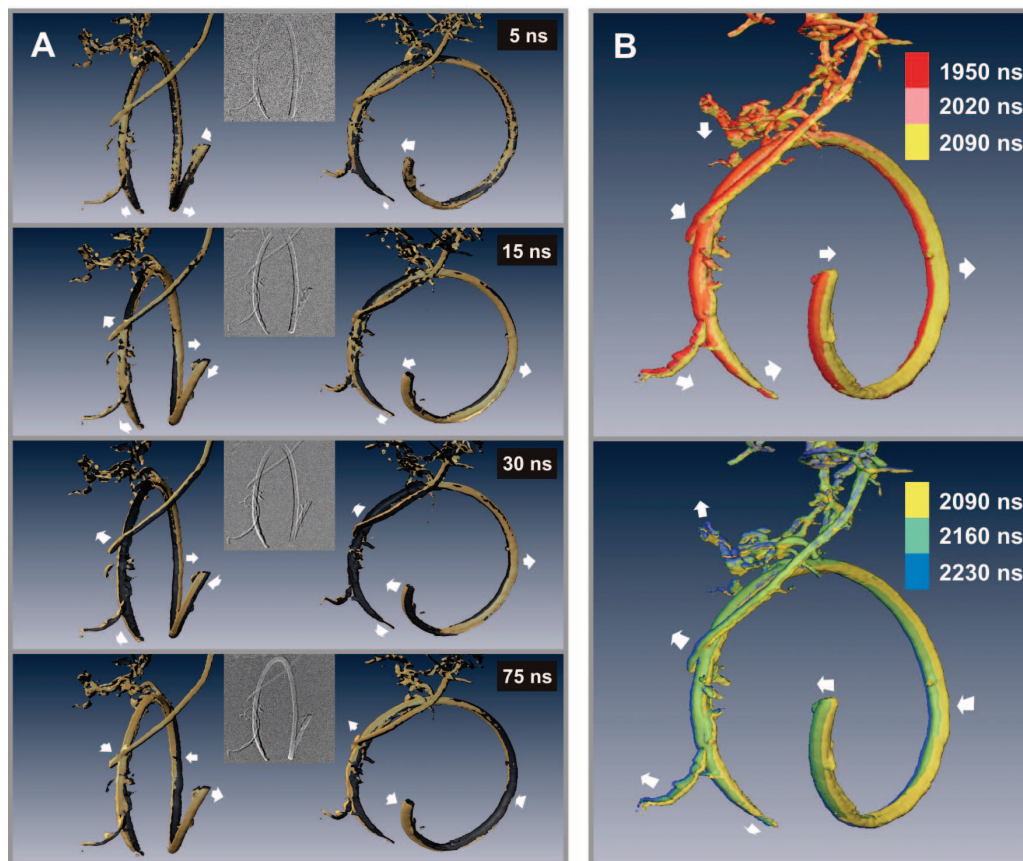


Fig. 4. 4D tomographic visualization of motion. **(A)** Representative 3D volume snapshots of the nanotubes at relatively early times. Each 3D rendered structure at different time delay (beige) is shown at two view angles. A reference volume model taken at $t = 0$ ns (black) is merged in each panel to highlight the resolved nanometer displacements. Arrows in each panel indicate the direction of motion. **(B)** The time-dependent structures visualized at later times and with various colors to indicate different temporal evolution. The wiggling motion of the whole bracelet is highlighted with arrows. From these tomograms, movies were constructed in the two different time domains (movies S2 and S3). Note that the time scale given here is chosen to display clearly the objects' motions, as opposed to the early ultrashort time domain (see text).



due to the wiggling motion of the ring that is supported by the bundle of nanotubes shown in the tomograms. Note that thermal vibrations (33) give rise, from room temperature to 1000°C, to amplitudes ranging from 0.5 to 1.0 nm, in contrast to the large amplitudes of tens of nanometers reported here for heating in the far-from-equilibrium state. In future work, it should be possible to map the microscopic forces involved by comparison with large-scale computer simulations of mechanical motions, including the influence of defects and fatigue on nanoscale materials properties.

4D electron tomography, which unites the power of volume imaging with time resolution, reveals the structural and morphological dynamics of a 3D object. In the application demonstrated here, for a complex ring structure in the non-equilibrium state, the tomographic movie displays the motions in different parts of the object on various time scales. The modes involved are those of breathing, due to segmental bending, and wiggling of the ring around the tethered position. Considering the three domains of electron microscopy—real space, Fourier space, and energy space—the introduction of energy resolution to tomography would constitute a fourth dimension of measurement (15), but here the integration of tomography with time represents the fundamental four coordinates of space and time. In this report, the proof-of-principle was made using stroboscopic ultrafast electron tomog-

raphy, but it should also be possible to use the technique of single-particle (tomographic) imaging together with single-pulse recording, provided that this recording is made before radiation damage can occur. The methodology promises to have wide-ranging applications in materials and biological sciences.

References and Notes

- P. A. Midgley, R. E. Dunin-Borkowski, *Nat. Mater.* **8**, 271 (2009).
- H. Friedrich, P. E. de Jongh, A. J. Verkleij, K. P. de Jong, *Chem. Rev.* **109**, 1613 (2009).
- V. Lucić, F. Förster, W. Baumeister, *Annu. Rev. Biochem.* **74**, 833 (2005) and references therein.
- R. McIntosh, D. Nicastro, D. Mastronarde, *Trends Cell Biol.* **15**, 43 (2005).
- J. Frank, Ed., *Electron Tomography: Methods for Three-Dimensional Visualization of Structures in the Cell* (Springer, New York, ed. 2, 2010) and references therein.
- D. J. De Rosier, A. Klug, *Nature* **217**, 130 (1968).
- R. A. Crowther, L. A. Amos, J. T. Finch, D. J. De Rosier, A. Klug, *Nature* **226**, 421 (1970).
- W. Hoppe, R. Langer, G. Knesch, C. Poppe, *Naturwissenschaften* **55**, 333 (1968).
- R. G. Hart, *Science* **159**, 1464 (1968).
- P. A. Midgley, E. P. W. Ward, A. B. Hungria, J. M. Thomas, *Chem. Soc. Rev.* **36**, 1477 (2007) and references therein.
- A. H. Zewail, J. M. Thomas, *4D Electron Microscopy: Imaging in Space and Time* (Imperial College Press, London, 2009) and references therein.
- P. W. Hawkes, J. C. H. Spence, Eds., *Science of Microscopy* (Springer, New York, 2006), vol. 1.
- P. A. Midgley, M. Weyland, *Ultramicroscopy* **96**, 413 (2003).
- J. J. Cha *et al.*, *Nano Lett.* **7**, 3770 (2007).
- M. H. Gass, K. K. K. Koziol, A. H. Windle, P. A. Midgley, *Nano Lett.* **6**, 376 (2006).
- C. Colliex *et al.*, *Philos. Trans. R. Soc. London Ser. A* **367**, 3845 (2009).
- J. M. Thomas *et al.*, *Angew. Chem. Int. Ed.* **43**, 6745 (2004).
- H. Li, H. L. Xin, D. A. Muller, L. A. Estroff, *Science* **326**, 1244 (2009).
- A. H. Zewail, *Science* **328**, 187 (2010) and references therein.
- B. Barwick, H. S. Park, O.-H. Kwon, J. S. Baskin, A. H. Zewail, *Science* **322**, 1227 (2008).
- O.-H. Kwon, B. Barwick, H. S. Park, J. S. Baskin, A. H. Zewail, *Nano Lett.* **8**, 3557 (2008).
- MWNTs (average diameter of 50 nm) were purchased and dispersed in cyclohexane. After ultrasonication, the solution was delivered to a bare copper grid (300 mesh), using a micropipette, and allowed to dry for immobilization of the tubes. MWNTs sitting on the middle of the grid square were selected to ensure the maximum range of tilt angles.
- Q. S. Zheng, M. B. Braumfeld, J. W. Sedat, D. A. Agard, *J. Struct. Biol.* **147**, 91 (2004).
- C. O. S. Sorzano *et al.*, *BMC Bioinformatics* **10**, 124 (2009).
- C. Messaoudi, T. Boudier, C. O. Sanchez Sorzano, S. Marco, *BMC Bioinformatics* **8**, 288 (2007).
- For structural change, the heating was carried out with excitation at 519 and 532 nm for 220-fs and 10-ns pulses, respectively. The fluence varied from 2.5 mJ/cm² (for femtosecond experiments) to 100 mJ/cm² (for nanosecond experiments); the repetition rate varied from 200 kHz to 3 kHz. Upon absorption of the pulse energy by the specimen, lattice phonons are formed in a few picoseconds (34). Consequently, the irradiated region heats up rapidly after phonon-phonon interactions on a time scale of tens of picoseconds. The initial temperature was deduced to be ~1000°C from knowledge of the optical and thermal properties of the specimen and the fluence, using a simple 1D heat-flow scheme (35). The impulsive thermal stress induces mechanical vibrations in the material, and the initial motions by heat-induced expansion are then transferred into longitudinal and flexural modes in 3D.

27. F. Banhart, *J. Mater. Sci.* **41**, 4505 (2006).
28. V. H. Crespi, N. G. Chopra, M. L. Cohen, A. Zettl, S. G. Louie, *Phys. Rev. B* **54**, 5927 (1996).
29. The extent of displacement may vary depending on the tilt angle, because the local thickness of the specimen along the axis of the excitation may change. However, the skin depth of the MWNT ring specimen for the 532-nm light is deduced to be $2\ \mu\text{m}$ [absorption coefficient $\alpha = 1.0 \times 10^4\ \text{cm}^{-1}$ (35)], which exceeds the largest local thickness along the ring specimen at a tilt angle of 35° . In addition, the absorption cross section of MWNTs is reported to be weakly dependent on the polarization of the incident beam for thick tubes (36). To further suppress any polarization dependence, we set the polarization of the optical excitation beam so that it was not along the long axis of the tube.
- Consequently, the heat gradient and thermal stress are uniform for the tilt angles recorded in this study.
30. P. Poncharal, Z. L. Wang, D. Ugarte, W. A. de Heer, *Science* **283**, 1513 (1999).
31. L. Meirovich, *Elements of Vibration Analysis* (McGraw-Hill, New York, ed. 2, 1986).
32. X.-L. Wei, Y. Liu, Q. Chen, M.-S. Wang, L.-M. Peng, *Adv. Funct. Mater.* **18**, 1555 (2008).
33. M. M. J. Treacy, T. W. Ebbesen, J. M. Gibson, *Nature* **381**, 678 (1996).
34. G. V. Hartland, *Annu. Rev. Phys. Chem.* **57**, 403 (2006).
35. T. Nakamiya *et al.*, *Thin Solid Films* **517**, 3854 (2009).
36. C. Ni, P. R. Bandaru, *Carbon* **47**, 2898 (2009).
37. S. Jonic, C. Vénien-Bryan, *Curr. Opin. Pharmacol.* **9**, 636 (2009).
38. Supported by NSF (grant DMR-0964886) and Air Force Office of Scientific Research (grant FA9550-07-1-0484) in the Physical Biology Center for Ultrafast Science and Technology supported by Gordon and Betty Moore Foundation at Caltech. A patent application has been filed by Caltech based on the methodology presented herein.

Supporting Online Material

www.sciencemag.org/cgi/content/full/328/5986/1668/DC1
Movies S1 to S3

5 April 2010; accepted 19 May 2010
10.1126/science.1190470

Measurement of the Instantaneous Velocity of a Brownian Particle

Tongcang Li, Simon Kheifets, David Medellin, Mark G. Raizen*

Brownian motion of particles affects many branches of science. We report on the Brownian motion of micrometer-sized beads of glass held in air by an optical tweezer, over a wide range of pressures, and we measured the instantaneous velocity of a Brownian particle. Our results provide direct verification of the energy equipartition theorem for a Brownian particle. For short times, the ballistic regime of Brownian motion was observed, in contrast to the usual diffusive regime. We discuss the applications of these methods toward cooling the center-of-mass motion of a bead in vacuum to the quantum ground motional state.

In 1907, Albert Einstein published a paper in which he considered the instantaneous velocity of a Brownian particle (1, 2). By measuring this quantity, one could prove that “the kinetic energy of the motion of the centre of gravity of a particle is independent of the size and nature of the particle and independent of the nature of its environment.” This is one of the basic tenets of statistical mechanics, known as the equipartition theorem. However, because of the very rapid randomization of the motion, Einstein concluded that the instantaneous velocity of a Brownian particle would be impossible to measure in practice.

We report here on the measurement of the instantaneous velocity of a Brownian particle in a system consisting of a single, micrometer-sized SiO_2 bead held in a dual-beam optical tweezer in air, over a wide range of pressures. The velocity data were used to verify the Maxwell-Boltzmann velocity distribution and the equipartition theorem for a Brownian particle. The ability to measure instantaneous velocity enables new fundamental tests of statistical mechanics of Brownian particles and is also a necessary step toward the cooling of a particle to the quantum ground motional state in vacuum.

The earliest quantitative studies of Brownian motion were focused on measuring velocities, and they generated enormous controversy (3, 4).

Center for Nonlinear Dynamics and Department of Physics, University of Texas at Austin, Austin, TX 78712, USA.

*To whom correspondence should be addressed. E-mail: raizen@physics.utexas.edu

The measured velocities of Brownian particles (3) were almost 1000-fold smaller than what was predicted by the energy equipartition theorem. Recent experiments with fast detectors that studied Brownian motion in liquid (5–7) and gaseous (8–10) environments observed nondiffusive motion of a Brownian particle.

Einstein’s theory predicts that $\langle[\Delta x(t)]^2\rangle = 2Dt$, where $\langle[\Delta x(t)]^2\rangle$ is the mean square displacement (MSD) in one dimension of a free Brownian particle during time t , and D is the diffusion constant (11). The diffusion constant can be calculated by $D = k_B T / \gamma$, where k_B is Boltzmann’s constant, T is the temperature, and γ is the Stokes friction coefficient. The mean velocity measured over an interval of time t is $\bar{v} \equiv \sqrt{\langle[\Delta x(t)]^2\rangle} / t = \sqrt{2D} / \sqrt{t}$. This diverges as t ap-

proaches 0 and therefore does not represent the real velocity of the particle (1, 2).

The equation $\langle[\Delta x(t)]^2\rangle = 2Dt$, however, is valid only when $t \gg \tau_p$; that is, in the diffusive regime. Here, $\tau_p = m/\gamma$ is the momentum relaxation time of a particle with mass m . At very short time scales ($t \ll \tau_p$), the dynamics of a particle are dominated by its inertia, and the motion is ballistic. The dynamics of a Brownian particle over all time scales can be described by a Langevin equation (12). The MSD of a Brownian particle at very short time scales is predicted to be $\langle[\Delta x(t)]^2\rangle = (k_B T/m)t^2$, and its instantaneous velocity can be measured as $v = \Delta x(t)/t$, when $t \ll \tau_p$ (13).

For a 1- μm -diameter silica (SiO_2) sphere in water, τ_p is about 0.1 μs and the root mean square (rms) velocity is about 2 mm/s in one dimension. To measure the instantaneous velocity with 10% uncertainty, one would require 2-pm spatial resolution in 10 ns, far beyond what is experimentally achievable today (7). Because of the lower viscosity of gas, compared with liquid, the τ_p of a particle in air is much larger. This lowers the technical demand for both temporal and spatial resolution. The main difficulty of performing high-precision measurements of a Brownian particle in air, however, is that the particle will fall under the influence of gravity. We overcome this problem by using optical tweezers to simultaneously trap and monitor a silica bead in air and vacuum, allowing long-duration, ultra-high-resolution measurements of its motion.

Fig. 1. Simplified schematic showing the counterpropagating dual-beam optical tweezers, and a novel detection system that has a 75-MHz bandwidth and ultralow noise. The s -polarized beam is reflected by a polarizing beam-splitter cube after it passes through a trapped bead inside a vacuum chamber. For detection, it is split by a mirror with a sharp edge. The p -polarized beam passes through the cube.

